PHYSICAL REVIEW B **108**, 115416 (2023)

Temperature-dependent terahertz properties of carriers and phonons in the topological Dirac semimetal Cd_3As_2

Lei Hou,[1] Yunkun Yang,[2,3] Aolong Li,[2] Qiujin Wang,[1] Qinan Li,[1] Min Wu,[1] Pengcheng Ji,[1] Yujun Zhang,[1]
Yiming Xiao,[1] Wen Xu,[4,1,5] Faxian Xiu,[2,*] and Lan Ding[1,†]
[1]*School of Physics and Astronomy and Key Lab of Quantum Information of Yunnan Province,*
Yunnan University, Kunming 650091, China
[2]*State Key Laboratory of Surface Physics and Department of Physics, Fudan University, Shanghai 200433, China*
[3]*Beijing Academy of Quantum Information Sciences, Beijing 100193, China*
[4]*Micro Optical Instruments, Inc., Shenzhen 518118, China*
[5]*Key Laboratory of Materials Physics, Institute of Solid State Physics, Chinese Academy of Science, Hefei 230031, China*

(Received 16 April 2023; revised 28 July 2023; accepted 30 August 2023; published 12 September 2023)

As a three-dimensional (3D) analog of graphene, the cadmium arsenide (Cd_3As_2) based topological Dirac semimetal has attracted enormous research interest recently. In this work, the temperature-dependent terahertz (THz) properties of Cd_3As_2 prepared epitaxially are investigated by using THz time-domain spectroscopy. In the regime of $1.5 \sim 300$ K, we obtain the optical conductivity of Cd_3As_2 and observe a remarkable phonon absorption peak in the range of $1.7 \sim 1.8$ THz. More importantly, it is demonstrated that the effects of weak electronic confinement and optical-phonon-limited behavior of carriers are dominated below and above $\sim$60 K, respectively. The weak electronic confinement can be attributed to the diffusive restoring current in polycrystalline grains of Cd_3As_2. Based on the Drude-Lorentz formula and the modified Drude-Smith formula, the temperature dependencies of the characteristic parameters are extracted to describe the carrier and phonon behaviors. These results not only can provide detailed knowledge of the THz response of epitaxially grown Cd_3As_2 depending on temperature but also may find applications in optoelectronic devices based on 3D Dirac semimetals.

DOI: 10.1103/PhysRevB.108.115416

I. INTRODUCTION

Three-dimensional (3D) Dirac semimetals, possessing a similar band structure to graphene but in the bulk form [1], have attracted a lot of research interest due to the striking features [2,3], such as the quantum Hall effect based on Weyl orbits [4], the chiral anomaly [5], and the two-dimensional topological insulator state [6]. This kind of Dirac system can be viewed as two copies of Weyl systems, in which there are two sets of the linear dispersion bands at each Dirac node with opposite chiral charge. These fourfold-degenerate 3D linear band crossings are protected by lattice point-group symmetries [7]. Several material systems have been proposed to realize 3D Dirac semimetals, such as Na_3Bi [8], β-BiO_2 [1], and Cd_3As_2 [9]. Among them, epitaxially grown thin films of Cd_3As_2 are widely investigated in experiments owing to their excellent preparation quality, stability, and large area. Besides the appealing electronic properties obtained by transport measurements [10–14], some of the most significant study on the exotic phenomena of Cd_3As_2 come through their response to electromagnetic/optical fields [15–19].

Because the photon energy is only several milli-electron-volts, terahertz (THz) spectroscopy is expected to be a powerful optical approach to reveal the features of Dirac fermions or carriers near the Fermi surface in 3D Dirac semimetals, as well as the characteristics of elementary excitations such as phonons and plasmons. For example, an anomalous electron-optical phonon coupling reduction and a bottleneck slowing of hot optical phonon relaxation was observed in Cd_3As_2 [20]. G. Ma and co-workers found a THz photoconductivity relaxation process in Cd_3As_2 film, which was dominated by the electron-hole recombination and mediated by the phonon-phonon scattering [21]. Furthermore, a large effective phonon magnetic moment [22] and the chiral anomaly [5] in the Cd_3As_2-based 3D semimetal were revealed by using the magnetoterahertz spectroscopy. Recently, a THz active metamaterial based on Cd_3As_2 film was also proposed and experimentally investigated [23]. By using broadband multi-THz spectroscopy, R. Matsunaga's group observed stimulated Rayleigh scattering enhanced by a longitudinal plasma mode in a periodically driven Cd_3As_2 film [24]. In the multi-THz region, they also investigated and resolved ultrafast dynamics of the photoexcited nonthermal electrons in thin films of Cd_3As_2 excited by near-infrared light [25]. For short, most of these works mainly focused on carrier dynamics and electron-phonon coupling in nonequilibrium-state (i.e., photoexcited) Cd_3As_2-based semimetals at some temperatures. However, more detailed knowledge about the temperature-dependent THz response of equilibrium-state Cd_3As_2, especially for the situations below 77 K and in a broad enough temperature range, has not been fully explored until now. In addition, in experimental research and device

---

[*] faxian@fudan.edu.cn

[†] dinglan@ynu.edu.cn

applications of 3D Dirac semimetals, epitaxially grown thin films of Cd_3As_2 are widely used owing to their excellent preparation quality, stability, and large area. Nevertheless, we still know little about the effects of intrinsic optical phonons (lattice modes) and polycrystalline grains induced by the epitaxial growth on the carrier behaviors in Cd_3As_2.

In this work, we measure the temperature-dependent THz conductivity of the Cd_3As_2-based Dirac semimetal prepared epitaxially in the range of 1.5 to 300 K. The effects of intrinsic optical phonons and polycrystalline grains on the carrier behaviors are investigated. It is found that the weak electronic confinement contributes obviously below ~60 K and in the low-frequency regime, whereas the electron mobility is limited by the optical phonon above ~60 K. The electronic confinement can be attributed to diffusive restoring current in the polycrystalline grains of Cd_3As_2. Moreover, the behaviors of carriers and phonons can be well described by the Drude-Lorentz formula and the modified Drude-Smith model, in which the characteristic parameters are extracted at different temperature. These results can deepen our understanding of the carrier and phonon behaviors in realistic topological Dirac semimetals in the equilibrium state and clarify the effects of temperature on these features.

II. SAMPLE PREPARATION AND THz MEASUREMENT

In our study, the Cd_3As_2 thin film with a thickness of 100 nm was prepared on sapphire substrate in a Perkin-Elmer (Waltham, MA, USA) 425B molecular beam epitaxy (MBE) system. Before transfer in the ultrahigh vacuum chamber of MBE 425B, the sapphire substrate with a thickness of 500 μm was degreased in acetone, methanol, and isopropanol in turn and then blown dry with N_2 to get a fresh surface. Afterward, the substrate was annealed at 550 °C for 30 min to remove the absorbed oxygen or water molecules. Next, high-purity Cd (99.9999%) and Te (99.9999%) were evaporated from standard Knudsen cells to synthesize the buffer layer CdTe. The flux of Te was overdosed. Finally, Cd_3As_2 bulk material (99.9999%, American Elements Inc., Los Angeles, CA, USA) was vaporized from the effusion cells and then deposited onto the CdTe layer. The thickness and growth quality of the thin film was *in situ* monitored by the reflection high-energy electron diffraction (RHEED) system during the whole process. Note that the Cd_3As_2 thin film obtained here is polycrystalline with a preferred in-plane orientation and grain boundaries, which is similar to the samples investigated in our previous works [20,21,23].

The temperature-dependent THz response of the sample is measured by using a THz time-domain spectroscopy (THz-TDS) system in conjunction with a thermostat. The frequency range studied here is 0.30 ~ 2.0 THz, within which the systematic error (measurement uncertainty) is small enough. Further details can be found in Appendix A. At a given temperature, the THz pulses transmitted through the sample (Cd_3As_2/sapphire) and through the bare sapphire substrate are measured as the sample and reference signals, respectively. Based on the Fourier transformation of these two time-domain signals, we can derive the complex electric fields in the frequency domain for the sample and reference, i.e., $E_{\mathrm{sam}}(\omega)$ and $E_{\mathrm{ref}}(\omega)$, respectively. Therefore, the relative THz transmission spectra of Cd_3As_2 can be obtained by $T(\omega) = E_{\mathrm{sam}}(\omega)/E_{\mathrm{ref}}(\omega)$, where $E_{\mathrm{ref}}(\omega)$ is found to be nearly independent of temperature. Then, we calculate the relative amplitude $|T(\omega)|$ and the phase change $\arg[T(\omega)]$ for the Cd_3As_2 film with increasing temperature, as shown in Figs. 1(a) and 1(b). Based on $T(\omega)$, we can extract the optical conductivity through the Tinkham formula [26,27]:

$$\sigma(\omega) = \sigma_{\mathrm{r}}(\omega) + i\sigma_{\mathrm{i}}(\omega) = \frac{1+\tilde{n}}{T(\omega)Z_0} - \frac{1+\tilde{n}}{Z_0}, \qquad (1)$$

in which $\tilde{n} \approx 2.85 + i0$ is the complex refractive index of the sapphire substrate measured by our THz-TDS system (see Appendix B), and $Z_0 = 377\ \Omega$ is the impedance of the free space. Then, the real (σ_{r}) and the imaginary (σ_{i}) parts of the optical conductivity at different temperature are obtained and shown in Figs. 1(c) and 1(d). Obviously, a remarkable absorption peak can be observed in the range of 1.7 ~ 1.8 THz in $\sigma_{\mathrm{r}}(\omega)$, which is attributed to electron-phonon interaction and will be discussed in detail later.

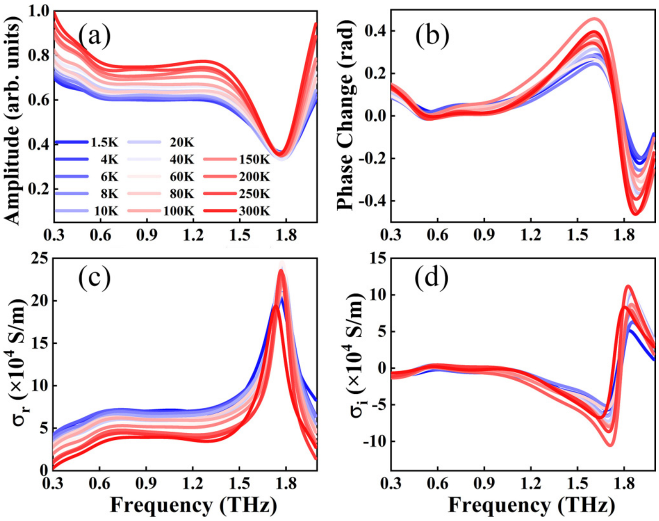

FIG. 1. Temperature-dependent THz response of the Cd_3As_2 film (100 nm). The (a) amplitude and (b) phase change of the relative THz transmission are given in the range of 0.3 ~ 2.0 THz. The (c) real and (d) imaginary parts of the optical conductivity are also extracted and shown. Note that the THz frequency is defined as $f = \omega/2\pi$.

III. RESULTS AND DISCUSSION

To our knowledge, the THz responses of semimetals are usually described by the Drude formula based on the free-electron-gas approximation [28–31], in which the real part of optical conductivity decreases monotonically with increasing frequency while the imaginary part should be positive. In contrast, most of the experimental data shown in Figs. 1(c) and 1(d) do not follow this rule, which means that it is impossible to reproduce the behavior of $\sigma(\omega)$ by only using the conventional Drude formula. When the frequency increases in the range of about $\omega/2\pi < 0.6$ THz, one can observe a slight increase of $\sigma_{\mathrm{r}}(\omega)$ and negative values of $\sigma_{\mathrm{i}}(\omega)$. In Fig. 1, we cannot find any features of absorption peaks in the range of 0.6 to 0.9 THz, such as a falling edge. Accordingly, this indicates that the optical phonon at around 0.7 THz reported previously [5,22] is very weak and thereby dominated by the contribution of carriers and the phonon mode in 1.7 ∼ 1.8 THz. This explanation will be confirmed later, while the 0.7 THz phonon mode is shown in Appendix C. Herein, the increasing $\sigma_\mathrm{r}(\omega)$ and negative $\sigma_\mathrm{i}(\omega)$ in the low-frequency range are typical features of weak confinement of carriers (i.e., carrier localization) and can be described by the conventional/modified Drude-Smith formula [32–36]. In essence, these spectral features are the result of the blueshift of the zero-frequency peak of the Drude response. Since our sample of $\mathrm{Cd_3As_2}$ is n type and the carriers are mainly electrons, the weak confinement of free electrons is also known as weak electronic confinement (WEC).

In the range of about 1.3 ∼ 2.0 THz, we find that the spectra of $\sigma_\mathrm{r}(\omega)$ and $\sigma_\mathrm{i}(\omega)$ are dominated by the resonance of a Lorentzian oscillator, which is induced by the absorption of optical phonons. The central frequency of this phonon mode is located in the range of 1.7 ∼ 1.8 THz and it does not decay and vanish with increasing temperature within 1.5 ∼ 300 K. Therefore, this phonon can be identified as a conventional optical phonon mode rather than the so-called helix vacancy-induced phonon mode [37]. Between these two regions, i.e., 0.6 ∼ 1.3 THz, one can attribute the relatively smooth conductivity curves to the contributions from the conventional Drude term and the Lorentzian oscillator mentioned previously. Therefore, in theory the whole spectrum of $\sigma(\omega)$ could be reproduced by a Drude-Smith-Lorentz model containing the conventional/modified Drude-Smith formula and a Lorentzian term. However, in practice this model is not very suitable to discuss the physics of the experimental results observed here. The reasons can be known as follows: (i) A complicated model with many terms and fitting parameters can reproduce nearly any experimental curves, which makes the model meaningless for analyzing the physical mechanism. (ii) From the view of spectral weight, the contribution of WEC is smaller than those of free carriers and the phonon especially in the high-frequency range, so it is unnecessary to describe the effects of WEC with the Drude-Smith formula in the presence of the phonon resonance in the range of 1.7 ∼ 1.8 THz.

In fact, the temperature-dependent behaviors of free carriers or phonons can also indirectly and qualitatively reflect the contribution of WEC. Accordingly, to reduce the degrees of freedom of the fitting process and to make the discussion clear, the optical conductivity of $\mathrm{Cd_3As_2}$ in the whole spectral range is mainly described by the Drude-Lorentz formula, whereas the WEC effect will be directly and quantitatively discussed by using the modified Drude-Smith formula only when the high-frequency (1.7 ∼ 1.8 THz) phonon resonance is subtracted from the measured data. The Drude-Lorentz formula can be expressed as

$$\sigma(\omega) = \epsilon_0\left[-\frac{\omega_\mathrm{p}^2}{i\omega - 1/\tau} - \frac{i\omega\Omega_\mathrm{s}^2}{\omega_0^2 - \omega^2 - i\omega/\tau_0} - i(\epsilon_\infty - 1)\omega\right], \tag{2}$$

where τ is the momentum scattering time of free carriers (i.e., free electrons here), $\omega_\mathrm{p} = \sqrt{Ne^2/\epsilon_0 m^*}$ is the plasma frequency with ϵ_0, N, and m^* respectively being the permittivity of free space, the electron density, and the effective electron mass, Ω_s is the strength of phonon oscillator, ω_0 is the central frequency of phonon resonance, and $1/2\pi\tau_0$ is the linewidth of phonon resonance. The background polarizability ϵ_∞ originates from absorptions above the measured spectral range including phonons and interband absorptions [5].

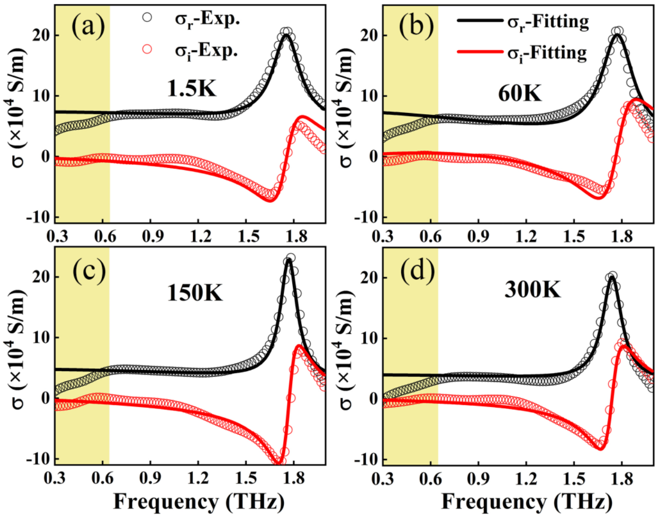

FIG. 2. Comparison of the measured and the fitted optical conductivity. The measured optical conductivity is fitted by the Drude-Lorentz formula and the situations of (a) $T = 1.5$ K, (b) 60 K, (c) 150 K, and (d) 300 K are shown as examples. The spectral range affected obviously by the WEC effect is filled with yellow.

By using Eq. (2), most of the experimental data can be reproduced well enough. The full comparison of the measured and the fitted optical conductivity at each temperature can be found in Appendix C. To avoid redundancy, Fig. 2 only presents the fitting results of 1.5, 60, 150, and 300 K as examples. Below ∼0.6 THz, the discrepancy between the experimental and the fitting results can be observed. As mentioned earlier, this is because Eq. (2) does not include the contribution of WEC, which affects the low-frequency domain more significantly than the high-frequency domain. In the experimental data, we also find that $\sigma_\mathrm{r}(\omega)$ increases slightly and $\sigma_\mathrm{i}(\omega)$ is negative but approaching 0 with increasing frequency. This means that the effect of the weak confinement of free electrons is not significant and thereby the discrepancy between the experimental and the fitting data does not affect the overall effectiveness of the Drude-Lorentz formula at most temperatures and frequencies.

Through the fitting process, the main characteristic parameters of carriers (electrons) and phonons are extracted and illustrated in Fig. 3. Note that the carriers are treated as free electrons and the WEC effect is not included in this model. Thus, the carrier parameters (ω_p and τ) obtained here are roughly estimated values, which will be modified by mainly considering the WEC effect later. For the carriers under the free-electron approximation, two temperature regimes can be distinguished in the dependencies of ω_p and τ upon temperature, i.e., $T < 60$ K and $T > 60$ K, as shown in Figs. 3(a) and 3(b). As we know, the thermal excitation of free carriers in semiconductors/semimetals usually leads to increased or nearly unchanged carrier density N, whereas the effective electron mass m^* is not sensitive to T. Thus, the

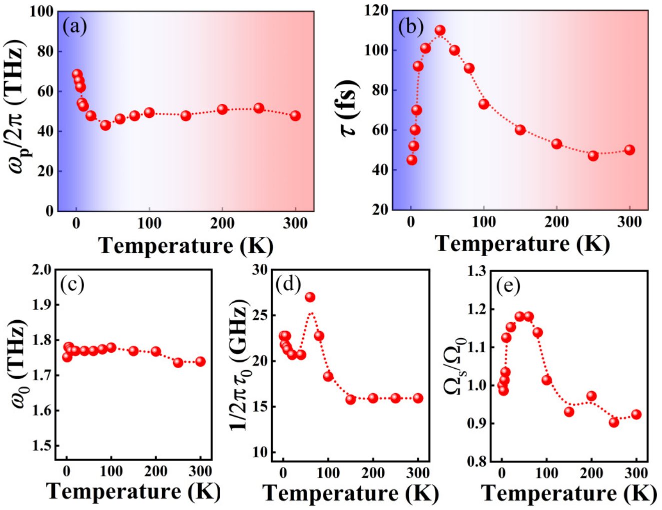

FIG. 3. Characteristic parameters. (a) The plasma frequency, (b) the scattering time of free carriers, (c) the central frequency of phonon, (d) the phonon linewidth, and (e) the strength of phonon oscillator depending on temperature. Note that the corresponding dotted curves are drawn to guide the eye. In (a) and (b), the temperature ranges affected mainly by the WEC effect ($T < 60$ K) and the optical-phonon-limited effect ($T > 60$ K) are filled with gradient blue and gradient red, respectively. The strength of phonon oscillator is normalized by the phonon strength for 1.5 K (Ω_0).

plasma frequency commonly is enhanced while the momentum scattering time decreases with increasing temperature. However, one can observe the contrary behaviors of ω_p and τ in the regime of $T < 60$ K, which could indirectly and qualitatively reflect the existence of WEC. Although the contribution of WEC is not included in Eq. (2) as an independent term, it in practice cannot be neglected entirely. For the high-frequency phonon resonance, the temperature-dependent parameters (ω_0, $1/2\pi\tau_0$, and Ω_s) are illustrated in Figs. 3(c)–3(e). In Cd_3As_2 films, two types of phonon absorptions above 1 THz were observed previously, including conventional optical phonons (F_0: 1.4 THz, F_2: 1.8 ∼ 1.9 THz) and helix vacancy-induced phonons (F_1: 1.7 ∼ 1.8 THz, F_3: 2.0 ∼ 2.1 THz) [37]. The latter ones usually decay and vanish quickly with increasing T. By considering the frequency range and the temperature dependence, the phonon resonance observed in 1.7 ∼ 1.8 THz here can be known as a conventional optical phonon that is more closed to the mode of F_2 (i.e., one of the A_{1g} modes). The slight shift of the frequency range of ω_0 may come from the differences of sample morphology or quality. When T changes from 1.5 K to ∼100 K, the central frequency is left nearly unchanged and the strength of the phonon oscillator shows a tendency of slight increase. As T increases from ∼100 K to 300 K, we find a slight redshift of ω_0 and a decrease tendency of Ω_s, which are typical features of optical phonon modes. In addition, a relatively complex relation between $1/2\pi\tau_0$ and T can be observed in the regime of 1.5 ∼ 100 K, whereas $1/2\pi\tau_0$ remains ∼15 GHz above ∼100 K. The temperature-dependent behaviors of the phonon parameters below ∼100 K are not regular, so one can infer that they may also be affected by WEC. The details of this process would be interesting but are beyond this work.

The mechanism of the WEC effect is briefly shown in Figs. 4(a)–4(c). It is known that the WEC effect usually occurs in nanostructure, nanostructure networks, and polycrystalline grains. Here, the Cd_3As_2 thin film grown epitaxially is polycrystalline rather than monocrystalline. From the atomic force microscopy (AFM) image and the TEM cross-section image, one can see the pattern of polycrystalline grains with a lateral scale of ∼50 nm to ∼1000 nm in the Cd_3As_2 film, which are introduced in the sample preparation process and can be treated as nanostructures. The electric field of the incident THz wave can induce the shift in average carrier (electron) position within the nanostructures (grains) of Cd_3As_2. Because most of the moving electrons are scattered or reflected by the grain boundaries, the electron position shift will result in a change of the electron density profile within each perturbation. Then, the electron density gradient can further give rise to carrier diffusion and thereby form diffusive restoring current [35], which weakly confines the moving electrons in the polycrystalline grains. As a result, the free electrons that respond the THz wave are reduced, leading to the increase of τ and the decrease of N and ω_p. In other words, the WEC effect mainly changes the overall THz response of free carriers. Although the contribution of WEC is qualitatively indicated by the behaviors of ω_p and τ of free electrons shown in Figs. 3(a) and 3(b), we still have little knowledge about the details of this physical process. As mentioned previously, in order to analyze the contribution of WEC quantitatively, we subtract the optical phonon resonance from the measured optical conductivity, as shown in the inset of Fig. 4(f) and Fig. 9 in Appendix C, and then model the optical conductivity by using the modified Drude-Smith formula:

$$\sigma(\omega) = \frac{\omega_p'^2 \epsilon_0}{1/\tau' - i\omega}\left(1 - \frac{C}{1 - i\omega t_{\mathrm{diff}}}\right), \tag{3}$$

in which ω_p' and τ' are the modified plasma frequency and the modified momentum scattering time of carriers affected by the WEC effect, respectively, t_{diff} is the diffusion time of electrons forming the diffusive restoring current, and $C = [0, 1]$ is the confinement factor used to phenomenologically measure the contribution of WEC. The parameter C is dependent on the size of a single nanostructure and its boundary reflectivity. In our sample, the polycrystalline grains are not isolated and discretely distributed, so the boundary reflectivity should approach but not reach 100%. This means that a very small portion of carriers can pass through the grain boundaries, which leads to $C \neq 1$ and $C \rightarrow 1$. Interestingly, after the subtraction of the high-frequency (1.7 ∼ 1.8 THz) phonon resonance, we can find the small phonon absorption peak at about 0.7 THz that is reported in some previous works [5,22], as illustrated in Fig. 9 in Appendix C. Because the phonon resonance in the range of 1.7 ∼ 1.8 THz has been removed and the 0.7 THz phonon resonance is weak enough, the experimental data can be fitted well by Eq. (3). The examples of the fitted $\sigma(\omega)$ are shown in the inset of Fig. 4(g), while detailed fitting results can be found in Appendix C. Moreover, in the absence of the high-frequency phonon mode, one can find that the frequency response of σ_r is a smooth peak with very broad full width that comes from the blueshift of the zero-frequency peak of the Drude response. This also confirms the validity

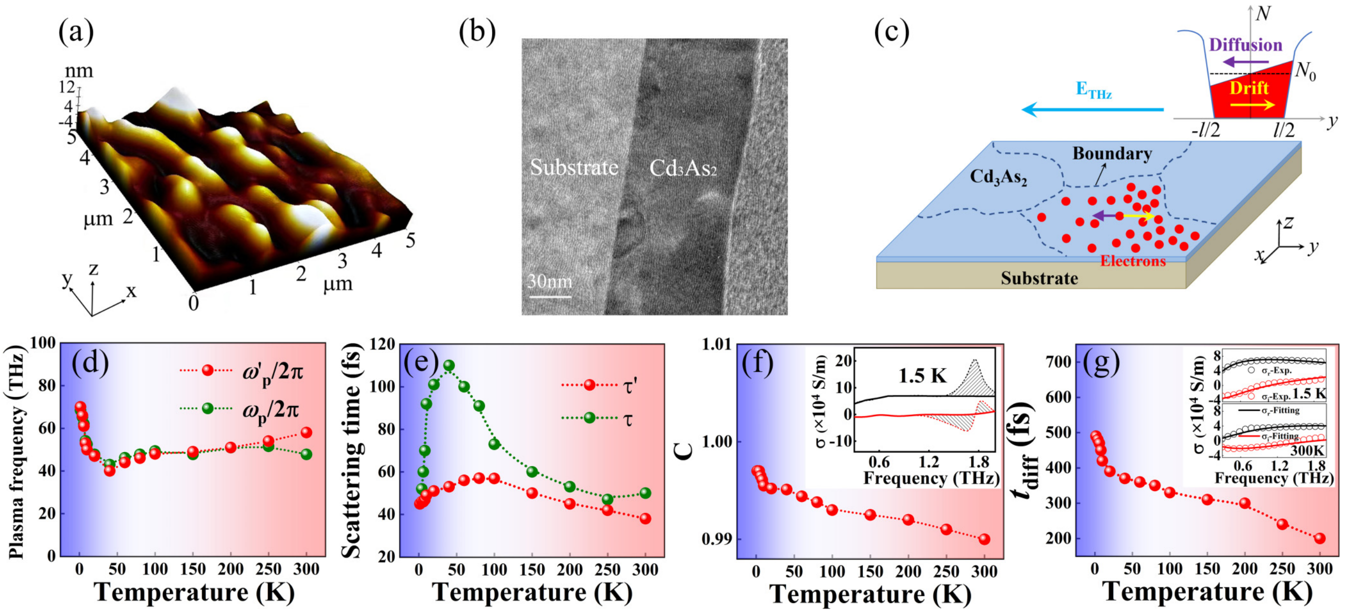

FIG. 4. Weak electronic confinement. (a) AFM image of the surface topography and (b) TEM cross-section image of the epitaxially prepared Cd_3As_2. (c) Schematic of the WEC effect induced by diffusive restoring current. The red circles denote free electrons in a surface perturbation or in a single-crystalline domain of Cd_3As_2 film. The inset of (c) presents the gradient in the electron density profile induced by the incident THz electric field $\mathbf{E}_{\mathrm{THz}}$, in which l denotes the average scale of the surface perturbation or single-crystalline domain. The temperature-dependent (d) modified plasma frequency, (e) modified scattering time, (f) confinement factor, and (g) diffusion time are obtained by fitting the experimental data (subtracting the optical phonon mode in the range of 1.7 ∼ 1.8 THz) with the modified Drude-Smith formula. The plasma frequency and the scattering time extracted based on Eq. (2) are also presented here for comparison. Note that the corresponding dotted curves are drawn to guide the eye. The inset of (f) shows an example of the subtraction of the high-frequency phonon resonance from the experimentally measured conductivity, while two representative fitting results based on Eq. (3) are shown as the inset of (g). In (d) to (g), the temperature ranges affected mainly by the WEC effect ($T < 60$ K) and the optical-phonon-limited effect ($T > 60$ K) are filled with gradient blue and gradient red, respectively.

of the explanation based on WEC, as mentioned previously. Based on the fitting process, ω_p', τ', C, and t_{diff} are obtained and shown in Figs. 4(d)–4(g).

The plasma frequency and the scattering time of carriers can be modified by quantitatively considering the contribution of WEC. Figures 4(d) and 4(e) show the comparison of these two parameters obtained based on the free-electron approximation (ω_p and τ) and the consideration of WEC (ω_p' and τ'). It is obvious that the temperature dependencies of ω_p' and τ' are similar to those of ω_p and τ, respectively. For the plasma frequency, ω_p' is nearly the same as ω_p at most of temperatures. In contrast, the scattering time is affected significantly by WEC, which results in the discrepancy between τ' and τ, especially below ∼60 K. By comparing with the results of monocrystalline Cd_3As_2 samples, one can find that the range of the plasma frequency in this work (40 ∼ 70 THz) is in line with that of the monocrystalline samples (30 ∼ 76 THz) [38]. The scattering time obtained here (40 ∼ 60 fs) is 1 ∼ 2 orders of magnitude smaller than that of the monocrystalline samples (∼4.2 ps). This difference can be attributed to the increase of carrier scattering events induced by the WEC effect in polycrystalline grains. It should also be noted that large-area Cd_3As_2 films, such as the epitaxially grown sample here, usually have more complex structure than single crystals of Cd_3As_2. Thus, one may find from previous works that large-area Cd_3As_2 films even prepared by the same method are more or less different in the characteristic parameters. However, the temperature dependencies of their THz properties should be similar, especially for the films grown by using the same approach.

Below ∼60 K, the contribution of WEC always exceeds that of the thermal excitation of free electrons, so the increasing T leads to rapid carrier diffusion and enhanced diffusive restoring current, which can boost the WEC effect. As a result, one can observe the decrease of ω_p'. Furthermore, it is known that the thermal motion of carriers is usually enhanced with T, corresponding to the thermal velocity $v_{\mathrm{th}} = \sqrt{k_B T/m^*}$. Thus, as T increases from 1.5 K to ∼60 K, the weakly confined electrons are easier to pass through the grain boundaries, which induces the increase of τ'. When the temperature exceeds ∼60 K, the accelerated thermal motion of carriers and the strong thermal excitation of free electrons can suppress the contribution of WEC. Accordingly, the slight increase of ω_p' and the decrease of τ' can be obtained, corresponding to the conventional behaviors in semiconductors/semimetals. In addition, the effect of electron-phonon interaction becomes more and more significant with T in the regime of $T > 60$ K, which is crucial for the determination of electron mobility and will be discussed later.

The confinement factor C and the diffusion time t_{diff} are two key parameters to directly investigate the WEC effect. As depicted in Figs. 4(f) and 4(g), both of them monotonically decrease with increasing T. Since the thermal motion of carriers speeds up with T, t_{diff} reduces rapidly associated with the

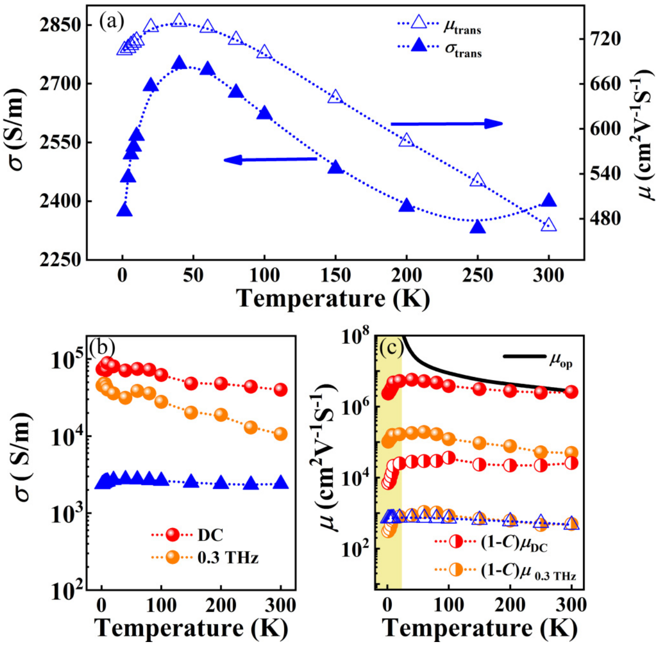

FIG. 5. (a) The DC conductivity and mobility obtained by electric transport measurements. Comparison of (b) the real part of σ and (c) the corresponding mobility obtained by THz measurements and transport measurements. The solid curve in (c) shows the optical-phonon-limited mobility of Dirac fermions calculated theoretically. All of the dotted curves are drawn to guide the eye.

enhancement of diffusive restoring current. Simultaneously, the larger thermal velocity $v_{\rm th}$ at higher temperature gives rise to the decrease of electron reflectivity on the grain boundaries and thereby leads to more carriers passing through the boundaries. As a result, C deviates from 1 with increasing T.

To discuss the electron-optical phonon interaction in Cd_3As_2 above ~60 K, Fig. 5 presents the temperature dependencies of $\sigma_{\rm r}$ and the electron mobility μ obtained based on electric transport and THz measurements. As a start, the results measured electrically are illustrated in Fig. 5(a) as references for further comparison. Next, by treating carriers as a gas of free electrons, the DC conductivity and the DC mobility corresponding to our THz experiment are calculated by $\sigma_{\rm DC} = \omega_{\rm p}^2 \tau \epsilon_0$ and $\mu_{\rm DC} = e\tau/m^*$, respectively. Note that the effective electron mass is fixed as $m^* \approx 0.03 m_{\rm e}$ based on the approximation of Dirac fermions [22,23], where $m_{\rm e}$ is the electron mass. Due to the gap between the ideal assumption and the actual situation, one can see from Fig. 5(b) and 5(c) that both $\sigma_{\rm DC}$ and $\mu_{\rm DC}$ are nearly two orders of magnitude larger than $\sigma_{\rm trans}$ and $\mu_{\rm trans}$ obtained by transport measurements. Even if we take the Smith correction based on the confinement factor C into account [39], the effective DC mobility $(1-C)\mu_{\rm DC}$ is still one order of magnitude larger than $\mu_{\rm trans}$. In fact, the DC situation of zero frequency cannot be realized in THz measurements, whereas the case of the lowest reliable frequency 0.3 THz is more realistic. Thus, we also provide the 0.3 THz conductivity, electron mobility, and effective mobility as $\sigma_{0.3\,{\rm THz}} = \sigma_{\rm r}(\omega/2\pi = 0.3\ {\rm THz})$, $\mu_{0.3\,{\rm THz}} = \sigma_{0.3\,{\rm THz}}/Ne$, and $(1-C)\mu_{0.3\,{\rm THz}}$, respectively. Because the electrons driven by THz field are much easier to pass through the boundaries of the polycrystalline grains than the electrons under DC electric field, we can find that $\sigma_{0.3\,{\rm THz}}$ and $\mu_{0.3\,{\rm THz}}$ are larger than $\sigma_{\rm trans}$ and $\mu_{\rm trans}$. In contrast, the effective mobility of 0.3 THz modified by the Smith correction, i.e., $(1-C)\mu_{0.3\,{\rm THz}}$, is in good agreement with $\mu_{\rm trans}$, as shown in Fig. 5(c). Moreover, from ~60 K to 300 K, the decreasing mobilities can be ascribed to the limitation of electron-optical phonon interaction and are restricted by the optical-phonon-limited mobility. To calculate the upper bound of μ, we assume that the electron-optical phonon coupling is unscreened and the Boltzmann transport equation is followed in the relaxation time approximation [40]. Therefore, the optical-phonon-limited mobility can be theoretically estimated by

$$\mu_{\rm op} \propto \frac{k_{\rm B}T}{\hbar\omega_0}\,\frac{\hbar^3 N^{1/3}}{e(\hbar\omega_0)m^{*2}}\,\frac{1}{N_{\rm op}(N_{\rm op}+1)}, \tag{4}$$

where $N_{\rm op} = [\exp(\hbar\omega_0/k_{\rm B}T) - 1]^{-1}$ is the phonon distribution function and $\hbar\omega_0$ is the optical phonon energy. In Fig. 5(c), the result of $\mu_{\rm op}$ is obtained by substituting the parameters shown in Fig. 3 into Eq. (4). For $T > 60$ K, the changing tendency of $\mu - T$, especially $\mu_{\rm DC} - T$, agrees well with that of $\mu_{\rm op} - T$. Meanwhile, the curve of $\mu_{\rm op} - T$ gradually approaches that of $\mu_{\rm DC} - T$ with increasing temperature, which determines the upper bound of μ. At lower temperatures, the obvious discrepancy between the experimental and theoretical data could be the result of the relatively weak electron–optical phonon interaction and the significant WEC effect.

In contrast to the widely used broadband spectral techniques such as FTIR spectroscopy, by using THz-TDS one can directly access the spectral amplitude and phase of the electric field rather than the intensity of the electromagnetic wave. This means that the complex dielectric function or the complex optical conductivity of a material can be measured by THz-TDS simultaneously [41]. In general, the effective or reliable bandwidth of a conventional THz-TDS system is smaller than ~3 THz (e.g., 1.7 THz here), which is narrower than some of other spectral techniques including FTIR spectroscopy. For the extraction of the fitting parameters, the relatively narrow bandwidth of THz-TDS may affect the accuracy of the results obtained based on fitting the Drude-type formula such as Eqs. (2) and (3). However, the imaginary part of optical conductivity (or the real part of dielectric function) can be directly measured by THz-TDS, which cannot be obtained by FTIR measurement unless using the Kramers-Kronig relation. Unlike the parameter extraction based on FTIR measurement, each group of the fitting parameters for THz-TDS is extracted from two sets of accurately measured data (e.g., the real and imaginary parts of optical conductivity) rather than only one set of directly measured data (e.g., the real part of optical conductivity). Therefore, this feature can compensate for the shortage of relatively narrow bandwidth of THz-TDS and thereby improve the reliability of the parameter extraction. In fact, THz-TDS has been demonstrated as a powerful method to obtain the optoelectronic parameters of materials [5,22,23,27,33,36,42] and an important complementary technique to FTIR spectroscopy [43–45]. Furthermore, since the photon energy of the electromagnetic wave below ~3 THz is small enough, the THz-TDS system in conjunction with a thermostat is very suitable to reveal the features of Dirac fermions or carriers near the Fermi surface of Cd_3As_2, as well as the characteristics of elementary excitations [5,22,23]. If spectral measurements with ultrabroad bandwidth and high-energy photons are applied, the electromagnetic response will be the result of more complex physical processes including significant contributions of carriers far away from the Dirac points and interband transition, which is beyond the scope of this work. In brief, the quality of our parameter extraction is consistent with previous works and the fitting parameters extracted from our THz measurements are reliable.

IV. CONCLUSIONS

In conclusion, by using THz-TDS we obtain the temperature-dependent optical conductivity $\sigma(\omega)$ of the 3D Dirac semimetal Cd_3As_2 prepared epitaxially. To describe the carrier and phonon properties, the optical conductivity is mainly fitted by the Drude-Lorentz formula and the characteristic parameters are also extracted. In the temperature range of $1.5 \sim 50$ K, one can find significant contribution of the WEC effect, which is induced by diffusive restoring current in the polycrystalline grains of Cd_3As_2. The mechanism of this effect is discussed by applying the modified Drude-Smith model to $\sigma(\omega)$ when the phonon resonance in the range of $1.7 \sim 1.8$ THz is subtracted. In the regime of $T > 60$ K, the optical-phonon-limited behavior of carriers is dominant and the upper bound of the corresponding optical-phonon-limited mobility is calculated theoretically. In addition, based on the measured optical conductivity and its theoretical model, one could easily investigate the distinctive plasmonic properties of Cd_3As_2, which would be affected by the phonons and the WEC effect. These significant results can deepen our understanding of the fundamental physics of realistic Cd_3As_2 films with polycrystalline grains. Moreover, the results may also find applications in designing and optimizing optoelectronic devices based on topological semimetals.

ACKNOWLEDGMENTS

This work was supported by the National Natural Science Foundation of China (Grants No. 12364033, No. U2230122, and No. U2067207), the Basic Research Project of Yunnan Province (Grant No. 202101AT070166), Shenzhen Science and Technology Program (Grant No. KQTD20190929173954826), and the Ten-Thousand Talents Program of Yunnan Province (Grant No. YNWR-QNBJ-2018-037).

The authors declare no conflicts of interest.

APPENDIX A

The THz-TDS system in conjunction with a thermostat is depicted in Fig. 6(a). The femtosecond laser with central wavelength of 800 nm (1.55 eV) and pulse duration of 35 fs was generated by a femtosecond laser amplifier (Coherent, Astrella, USA) with repetition rate of 1 kHz. This laser beam was split into a pump beam and a probe beam for THz generation and detection, respectively. Based on a ZnTe crystal, the pulsed THz wave was generated through optical rectification. The generated THz wave was focused on the Cd_3As_2 sample, which was fixed on a sample holder inside the thermostat (Oxford, Spectromag PT, UK) with two quartz windows. The vacuum degree inside the sample holder was maintained at about 10^{-7} bars, while the temperature was tuned in the range of $1.5 \sim 300$ K. Then, by using a standard electro-optic sampling technique, the THz wave transmitted through the sample or the reference (bare substrate) was detected. The time delay between the generation and probe pulses was controlled by dual retroreflectors driven by a servo. The reliable band of our experiment is $0.3 \sim 2.0$ THz, which was determined by the relative THz transmission amplitude based on two consecutive measurements without reference substrate and sample. In this band, the relative amplitude deviated less than ~1% away from 100%, as shown in Fig. 6(b). Based on this transmission uncertainty, the intrinsic/systematic error (uncertainty) of the THz measurements can be roughly evaluated. Specifically, if we translate the transmission uncertainty to the uncertainty in σ_r, the result is obtained as about $|\Delta_{\text{int}}| \leqslant 0.08 \times 10^4$ S/m through Eq. (1), as shown in Fig. 6(c). Therefore, the systematic error Δ_{int} is small enough and thereby affects the temperature-induced change of the THz response very weakly.

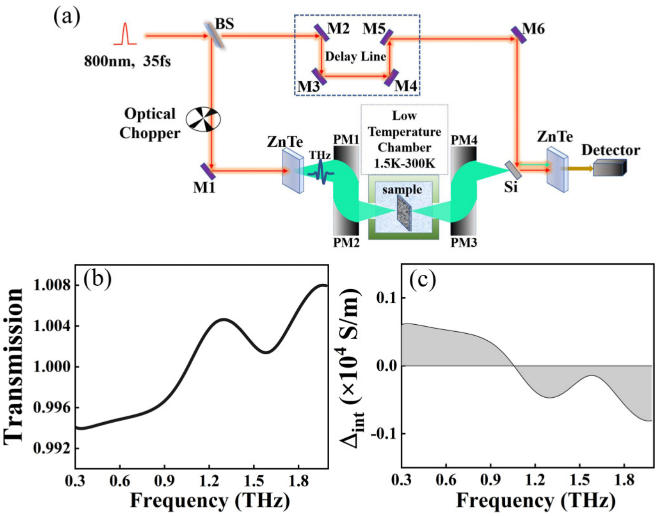

FIG. 6. (a) Schematic diagram of the THz-TDS system in conjunction with a thermostat. BS: Beam splitter; M1–6: metallic reflecting mirrors; PM1–4: off-axis parabolic mirrors. (b) The systematic deviation of the THz transmission and (c) the corresponding translated error in $\sigma_r(\omega)$ (systematic error).

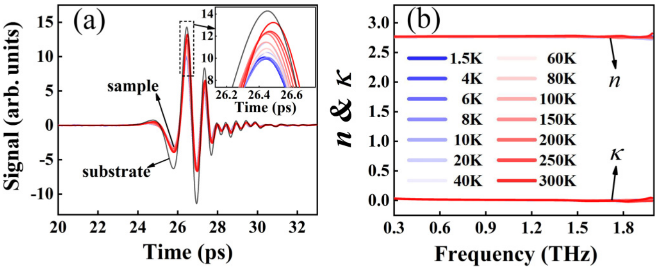

FIG. 7. (a) The THz pulses transmitted through the sample (Cd_3As_2/sapphire) and through the bare sapphire substrate at different temperature. The inset of (a) shows the local enlarged drawing of the signal peaks. (b) The temperature-dependent complex index of the sapphire substrate with thickness of 500 μm.

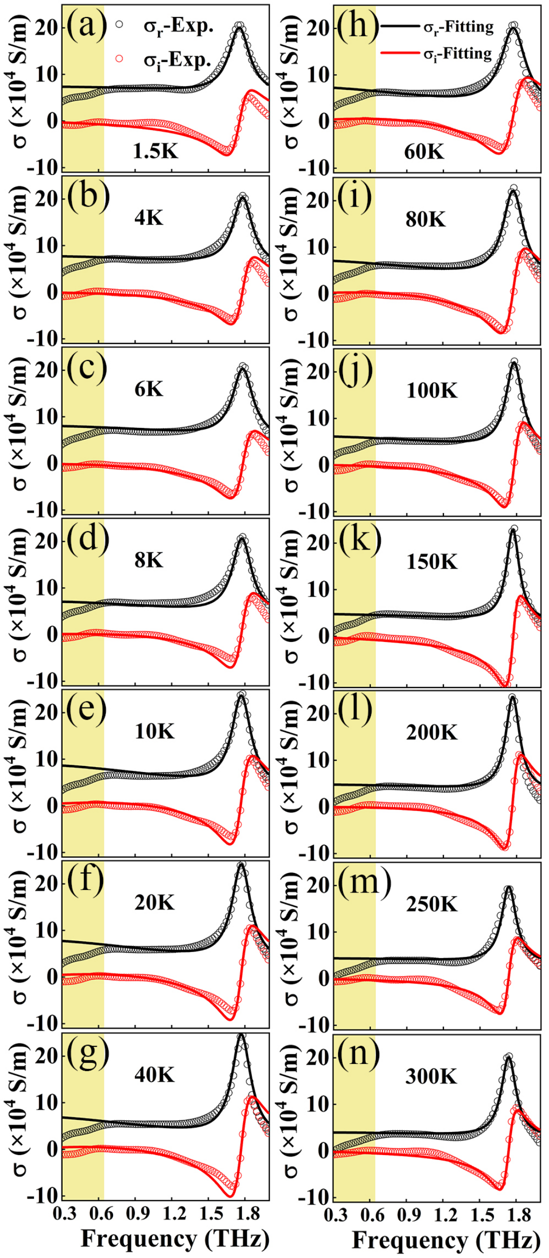

FIG. 8. Comparison of the measured and the fitted optical conductivity in the range of 0.30 ∼ 2.0 THz at (a) $T = 1.5$ K, (b) 4 K, (c) 6 K, (d) 8 K, (e) 10 K, (f) 20 K, (g) 40 K, (h) 60 K, (i) 80 K, (j) 100 K, (k) 150 K, (l) 200 K, (m) 250 K, and (n) 300 K. The measured optical conductivity is fitted by the Drude-Lorentz formula. The spectral range affected obviously by the WEC effect is filled with yellow.

APPENDIX B

The time-domain THz signals of the sample and the substrate at different temperature are illustrated in Fig. 7(a). As mentioned in Sec. II, the relative THz transmission spectra of Cd_3As_2 can be obtained based on the Fourier transformation of these pulses. To extract the optical conductivity of

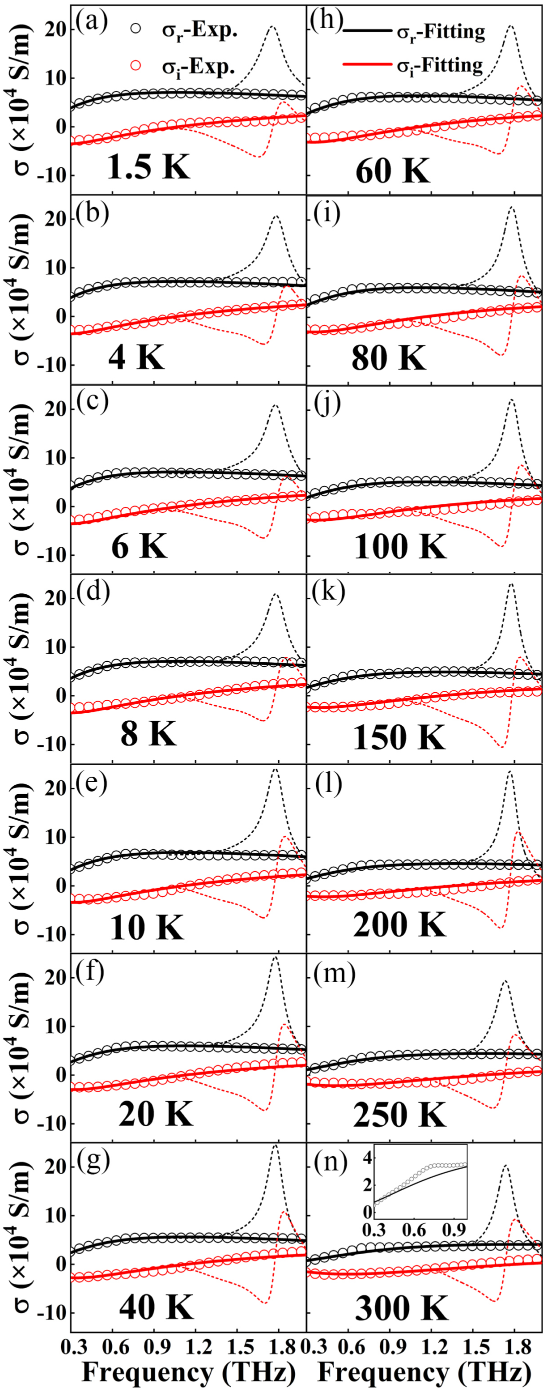

FIG. 9. The measured optical conductivity, in which the phonon mode in the range of 1.7 ∼ 1.8 THz has been subtracted, and the corresponding fitted data in the range of 0.30 ∼ 2.0 THz at (a) $T =$ 1.5 K, (b) 4 K, (c) 6 K, (d) 8 K, (e) 10 K, (f) 20 K, (g) 40 K, (h) 60 K, (i) 80 K, (j) 100 K, (k) 150 K, (l) 200 K, (m) 250 K, and (n) 300 K. The fitting is performed based on the modified Drude-Smith formula. Note that the dashed curves represent the optical phonon resonance in the range of 1.7 ∼ 1.8 THz subtracted from the measured data. The inset of (n) shows the local enlarged drawing of 0.3 to 0.95 THz, in which the weak optical phonon mode at around 0.7 THz can be observed.

the Cd_3As_2 film via Eq. (1), we also measured the complex refractive index of the sapphire substrate, as shown in Fig. 7(b). Obviously, the substrate is nearly lossless in THz range and its complex index is independent to temperature, so we use $\tilde{n} = n + i\kappa \approx 2.85 + i0$ in this work.

APPENDIX C

The optical conductivity of Cd_3As_2 in the whole spectral range (0.30 ∼ 2.0 THz) is mainly fitted by the Drude-Lorentz formula. The full comparison of the measured and the fitted optical conductivity at each temperature can be seen in Fig. 8, in which the contribution of WEC is indicated qualitatively in the range of $\omega/2\pi < 0.6$ THz. To quantitatively discuss the WEC effect, we subtract the optical phonon resonance (in 1.7 ∼ 1.8 THz) from the measured optical conductivity, and then reproduce the optical conductivity by using the modified Drude-Smith formula, as shown in Fig. 9. One can also find the weak optical phonon peak at ∼0.7 THz, which was reported previously [5,22].

[1] S. M. Young, S. Zaheer, J. C. Y. Teo, C. L. Kane, E. J. Mele, and A. M. Rappe, Phys. Rev. Lett. **108**, 140405 (2012).

[2] N. P. Armitage, E. J. Mele, and A. Vishwanath, Rev. Mod. Phys. **90**, 015001 (2018).

[3] C. Zhang, Y. Zhang, H.-Z. Lu, X. C. Xie, and F. Xiu, Nat. Rev. Phys. **3**, 660 (2021).

[4] C. Zhang, Y. Zhang, X. Yuan, S. Lu, J. Zhang, A. Narayan, Y. Liu, H. Zhang, Z. Ni, R. Liu, E. S. Choi, A. Suslov, S. Sanvito, L. Pi, H.-Z. Lu, A. C. Potter, and F. Xiu, Nature (London) **565**, 331 (2019).

[5] B. Cheng, T. Schumann, S. Stemmer, and N. P. Armitage, Sci. Adv. **7**, 0914 (2021).

[6] A. C. Lygo, B. Guo, A. Rashidi, V. Huang, P. Cuadros-Romero, and S. Stemmer, Phys. Rev. Lett. **130**, 046201 (2023).

[7] M. N. Ali, Q. Gibson, S. Jeon, B. B. Zhou, A. Yazdani, and R. J. Cava, Inorg. Chem. **53**, 4062 (2014).

[8] Z. Wang, Y. Sun, X. Q. Chen, C. Franchini, G. Xu, H. Weng, X. Dai, and Z. Fang, Phys. Rev. B **85**, 195320 (2012).

[9] Z. Wang, H. Weng, Q. Wu, X. Dai, and Z. Fang, Phys. Rev. B **88**, 125427 (2013).

[10] J. Cao, S. Liang, C. Zhang, Y. Liu, J. Huang, Z. Jin, Z.-G. Chen, Z. Wang, Q. Wang, J. Zhao, S. Li, X. Dai, J. Zou, Z. Xia, L. Li, and F. Xiu, Nat. Commun. **6**, 7779 (2015).

[11] P. J. W. Moll, N. L. Nair, T. Helm, A. C. Potter, I. Kimchi, A. Vishwanath, and J. G. Analytis, Nature (London) **535**, 266 (2016).

[12] P. Cheng, C. Zhang, Y. Liu, X. Yuan, F. Song, Q. Sun, P. Zhou, D. W. Zhang, and F. Xiu, New J. Phys. **18**, 083003 (2016).

[13] C. Zhang, A. Narayan, S. Lu, J. Zhang, H. Zhang, Z. Ni, X. Yuan, Y. Liu, J.-H. Park, E. Zhang, W. Wang, S. Liu, L. Cheng, L. Pi, Z. Sheng, S. Sanvito, and F. Xiu, Nat. Commun. **8**, 1272 (2017).

[14] L. Galletti, T. Schumann, D. A. Kealhofer, M. Goyal, and S. Stemmer, Phys. Rev. B **99**, 201401 (2019).

[15] M. Neupane, S.-Y. Xu, R. Sankar, N. Alidoust, G. Bian, C. Liu, llya Belopolski, T.-R. Chang, H.-T. Jeng, H. Lin, A. Bansil, F. Chou, and M. Z. Hasan, Nat. Commun. **5**, 3786 (2014).

[16] C. P. Weber, E. Arushanov, B. S. Berggren, T. Hosseini, N. Kouklin, and A. Nateprov, Appl. Phys. Lett. **106**, 231904 (2015).

[17] A. Akrap, M. Hakl, S. Tchoumakov, I. Crassee, J. Kuba, M. O. Goerbig, C. C. Homes, O. Caha, J. Novak, F. Teppe, W. Desrat, S. Koohpayeh, L. Wu, N. P. Armitage, A. Nateprov, E. Arushanov, Q. D. Gibson, R. J. Cava, D. van der Marel, B. A. Piot *et al.*, Phys. Rev. Lett. **117**, 136401 (2016).

[18] C. Zhu, F. Wang, Y. Meng, X. Yuan, F. Xiu, H. Luo, Y. Wang, J. Li, X. Lv, L. He, Y. Xu, J. Liu, C. Zhang, Y. Shi, R. Zhang, and S. Zhu, Nat. Commun. **8**, 14111 (2017).

[19] S. Yue, H. T. Chorsi, M. Goyal, T. Schumann, R. Yang, T. Xu, B. Deng, S. Stemmer, J. A. Schuller, and B. Liao, Phys. Rev. Res. **1**, 033101 (2019).

[20] W. Lu, J. Ling, F. Xiu, and D. Sun, Phys. Rev. B **98**, 104310 (2018).

[21] W. Zhang, Y. Yang, P. Suo, W. Zhao, J. Guo, Q. Lu, X. Lin, Z. Jin, L. Wang, G. Chen, F. Xiu, W. Liu, C. Zhang, and G. Ma, Appl. Phys. Lett. **114**, 221102 (2019).

[22] B. Cheng, T. Schumann, Y. Wang, X. Zhang, D. Barbalas, S. Stemmer, and N. P. Armitage, Nano Lett. **20**, 5991 (2020).

[23] Z. Dai, M. Manjappa, Y. Yang, T. C. W. Tan, B. Qiang, S. Han, L. Wong, F. Xiu, W. Liu, and R. Singh, Adv. Funct. Mater. **31**, 2011011 (2021).

[24] Y. Murotani, N. Kanda, T. N. Ikeda, T. Matsuda, M. Goyal, J. Yoshinobu, Y. Kobayashi, S. Stemmer, and R. Matsunaga, Phys. Rev. Lett. **129**, 207402 (2022).

[25] N. Kanda, Y. Murotani, T. Matsuda, M. Goyal, S. Salmani-Rezaie, J. Yoshinobu, S. Stemmer, and R. Matsunaga, Nano Lett. **22**, 2358 (2022).

[26] M. Tinkham, Phys. Rev. **104**, 845 (1956).

[27] Q. Wang, J. Qin, Y. Xiao, W. Xu, and L. Ding, Electronics **12**, 864 (2023).

[28] L. Ding, W. Xu, C. Zhao, S. Wang, and H. Liu, Opt. Lett. **40**, 4524 (2015).

[29] L. Ding, T. Qiu, J. Zhang, and W. Xu, J. Opt. **21**, 125602 (2019).

[30] J. Liu, L. Ding, C. Zhao, C. Liang, Y. Xiao, J. Zhang, and W. Xu, IEEE Photon. J. **11**, 4800708 (2019).

[31] L. Ding, T. Guo, J. Liu, and S. Zhou, Proc. SPIE **11194**, 111940H (2019).

[32] N. V. Smith, Phys. Rev. B **64**, 155106 (2001).

[33] C. Wang, W. Xu, H. Mei, H. Qin, X. Zhao, C. Zhang, H. Yuan, J. Zhang, Y. Xu, P. Li, and M. Li, Opt. Lett. **44**, 4139 (2019).

[34] T. Guo, L. Hou, W. Xu, Y. Xiao, and L. Ding, J. Opt. Soc. Am. B **39**, 1711 (2022).

[35] T. L. Cocker, D. Baillie, M. Buruma, L. V. Titova, R. D. Sydora, F. Marsiglio, and F. A. Hegmann, Phys. Rev. B **96**, 205439 (2017).

[36] K. P. Mithun, A. Kumar, S. Kundu, N. Ravishankar, and A. K. Sood, Phys. Rev. B **105**, 144302 (2022).

[37] F. Sun, Q. Wu, Y. L. Wu, H. Zhao, C. J. Yi, Y. C. Tian, H. W. Liu, Y. G. Shi, H. Ding, X. Dai, P. Richard, and J. Zhao, Phys. Rev. B **95**, 235108 (2017).

[38] I. Crassee, E. Martino, C. C. Homes, O. Caha, J. Novak, P. Tuckmantel, M. Hakl, A. Nateprov, E. Arushanov, Q. D.

Gibson, R. J. Cava, S. M. Koohpayeh, K. E. Arpino, T. M. McQueen, M. Orlita, and A. Akrap, Phys. Rev. B **97**, 125204 (2018).

[39] C. La-o-vorakiat, T. Salim, J. Kadro, M.-T. Khuc, R. Haselsberger, L. Cheng, H. Xia, G. G. Gurzadyan, H. Su, Y. M. Lam, R. A. Marcus, M.-E. Michel-Beyerle, and E. E. M. Chia, Nat. Commun. **6**, 7903 (2015).

[40] S. S. Kubakaddi, J. Appl. Phys. **126**, 135703 (2019).

[41] M. Koch, D. M. Mittleman, J. Ornik, and E. Castro-Camus, Nat. Rev. Methods Primers **3**, 48 (2023).

[42] L. Ding, M. Wu, S. Zhou, L. Zhu, H. Wen, X. Cheng, and W. Xu, Phys. Status Solidi RRL (2023).

[43] T. Wang, M. Zalkovskij, K. Iwaszczuk, A. V. Lavrinenko, G. V. Naik, J. Kim, A. Boltasseva, and P. U. Jepsen, Opt. Mater. Express **5**, 566 (2015).

[44] K. Arts, R. Vervuurt, A. Bhattacharya, J. G. Rivas, J. W. Oosterbeek, and A. A. Bol, J. Appl. Phys. **124**, 073105 (2018).

[45] A. Abouelsayed, B. Anis, and W. H. Eisa, J. Phys. Chem. C **124**, 18243 (2020).